Nonlinear Dyn (2023) 111:17687–17707
https://doi.org/10.1007/s11071-023-08808-w

ORIGINAL PAPER

Ultra-broad bandgap induced by hybrid hardening and softening nonlinearity in metastructure

Jianlei Zhao · Hao Zhou · Kaijun Yi · Ivana Kovacic · Rui Zhu

Received: 2 March 2023 / Accepted: 29 July 2023 / Published online: 24 August 2023

Abstract Metamaterials are artificial microstructured media that exhibit unique effective material properties and can be tailored to achieve negative properties that inhibit the propagation of acoustic or elastic waves. However, the effectiveness of linear metamaterials (LMs) based on resonance mechanisms is limited to a narrow frequency band. To overcome this limitation, nonlinear metamaterials (NLMs) have been investigated for enlarged bandwidth and wave phenomena beyond the linear systems. This paper presents a new mechanism for achieving an ultra-broad bandgap using a chain of triplets of resonators, based on the combination of hardening-plus-softening nonlinearity. The paper begins by investigating the bandgap and transmission characteristics of NLMs with different arrangements of single-hardening or single-softening nonlinear spring element. Explicit expressions for the nonlinear dispersion relations have been derived through a perturbation method. The paper then explores the combination of hardening-plus-softening nonlinearity to achieve an ultra-broad bandgap, which is more than twice as wide as the bandgap in the corresponding LM. The transmission characteristics are investigated analytically and validated numerically, providing evidence for the existence and accuracy of the predicted ultra-broad bandgap. The paper also examines nonlinear phenomena such as the dual wavevector and inflection point of transmissions in detail. Finally, the physical origin of the ultra-broad bandgap is elaborated through the nonlinear frequency response of a unit cell solved using a high-order harmonic balance method. The findings of this study are expected to provide a new strategy for broadening vibration suppression and offer new insight into the behavior of nonlinear periodic structures.

Keywords Nonlinear metamaterial · Ultra-broad bandgap · Hardening nonlinearity · Softening nonlinearity

List of symbols

A_1^0	Amplitude of incident wave
A_b	Excitation amplitude applied at the first unit cell in numerical analysis
a	Lattice constant
c_1	Secular terms
$c.c$	Complex conjugate
i	Imaginary unit $\sqrt{-1}$
k_1, k_2, k_3	Linear spring coefficient of unit cells from the external to the internal

J. Zhao · H. Zhou · K. Yi · R. Zhu (✉)
School of Aerospace Engineering, Beijing Institute of Technology, Beijing 100081, China
e-mail: ruizhu@bit.edu.cn

I. Kovacic (✉)
Faculty of Technical Science, Centre of Excellence for Vibro-Acoustic Systems and Signal Processing, University of Novi Sad, 21000 Novi Sad, Serbia
e-mail: ivanakov@uns.ac.rs

LM	Linear metamaterial
m_1, m_2,m_3	Discrete mass of unit cells from the external to the internal
n	Location number of unit cell
NLM	Nonlinear metamaterial
q	The wave number
T_l	Transmission for linear system
T_{nl}	Transmission for nonlinear system
u_1^n, u_2^n,u_3^n	Displacement of m_1,m_2, m_3 For the n^{th} unit cells
$u_j^{n(0)}$	The zero-order term of the perturbation expansion of the displacement
$u_j^{n(1)}$	The first-order term of the perturbation expansion of the displacement
x_i	The deformation of the corresponding spring

Greek letters

γ_2,γ_3	Non-dimensional nonlinear stiffness
δ_2,δ_3	Non-dimensional stiffness
ε	Perturbation parameter
θ_2,θ_3	Non-dimensional mass
κ	Dimensionless wave number
λ	Coefficient of
τ	Non-dimensional time
ω_0	Natural frequency
Γ_2,Γ_3	Nonlinear spring coefficients
Ω	Non-dimensional frequency
Ω_0	Zero-order term of the perturbation expansion of the non-dimensional frequency
Ω_1	First-order term of the perturbation expansion of the non-dimensional frequency
Ω_L^1	Lower edge frequency of the first bandgap
Ω_U^1	Upper edge frequency of the first bandgap
Ω_L^2	Lower edge frequency of second bandgap
Ω_U^2	Upper edge frequency of second bandgap
Ω_c	Cut-off frequency

1 Introduction

Breaking the limits of mechanical properties in engineered materials and structures is an eternal goal. Metamaterials, which are artificial microstructured materials with abnormal characteristics [1], offer a new perspective and motivation for achieving this goal. The periodic microstructure of metamaterials can be functionally customized to surpass the limits of properties found in natural materials, such as negative mass density/bulk modulus [2, 3], negative refraction [4], and odd elasticity [5, 6]. Metastructures, which are metamaterial-based structures with specified boundary conditions and finite structures, have a wide range of applications including suppressing noise and vibration [7–10], harvesting energy [11–13], shock absorption [14, 15], and waveguides [16, 17]. In particular, metamaterials and metastructures have been proven to be better suited for low-frequency vibration isolation than phononic crystals, mechanisms, and damping materials.

Currently, most studies focus on the linear locally resonant (LR)-based metamaterials, where the narrow bandgaps arise from the dynamic behavior of the linear local resonators. For single resonator systems, researchers mainly investigate the changes on the structural parameters of the resonator in order to achieve a broad bandgap. Concerning discrete mass-in-mass lattice systems, Tan et al. [18] demonstrated that increasing the mass ratio of the inner and outer masses is a way to maximize the bandgap. However, there is no significant increase in the negative effective mass quantity near the increased bandgap region. Hu et al. [19] showed that introducing internal couplings between neighboring local resonators in conventional mass-in-mass systems can achieve the maximum bandwidth. Regarding metamaterial-based continuous structures, Abdeljaber et al. [20] used optimization approaches to explore the interactions between parametric design and broadband vibration suppression in a 1D metamaterial beam embedded with chiral lattice resonators. Yeh et al. [21] developed a genetic algorithm to optimize the geometries of embedded viscoelastic resonators in a 1D metamaterial tube, maximizing the vibration attenuation region. Wang et al. [22] proposed a 2D tunable digital metamaterial consisting of primary lattices and auxiliary beams with electromagnets to achieve the maximum bandwidth. Yang et al. [23] proposed topology optimization of 2D ternary metamaterials, composed of core, coating, and matrix regions, by using the concept of effective mass density to maximize selected bandgaps. Active mechanisms are also explored to widen bandgaps. For example, Yi et al. [24] realized a large bandgap by tuning the shunting parameters of a piezoelectric metamaterial beam to have a graded variation pattern in space. Yi et al. [25] also proposed to include a negative capacitor into the original resonant circuit

and realized much wider bandgaps. For combined resonator systems, optimizing the number and arrangement of resonators is typically aimed at enlarging the bandgap. Tan et al. [18] proposed a dual-resonator mass-in-mass system for a wider bandgap by optimizing the negative effective mass density. Wu et al. [26, 27] developed and optimized multiple resonating mass-in-mass systems for continuous broad bandgaps by connecting multiple narrow bandgaps. Additionally, the impact of different connection methods on the number and width of band gaps was investigated [28–30], including in-parallel and in-series connections, or combinations of these, between the resonators and host components. In terms of metamaterial-based continuous structures, Zhu et al. [7] proposed a 1D chiral elastic metamaterial beam with section-distributed resonators and achieved broadband vibration suppression. Hu et al. [31] proposed a 1D metamaterial beam with a graded arrangement of local resonators for broadband vibration suppression. Celli et al. [32] investigated the effect of non-uniform spatial gradient and disorder distribution of resonators in 2D rainbow metamaterial plates to achieve bandgap widening through experiments. Li et al. [33] proposed a 2D stiffness-mass-coding metamaterial to achieve broadband tunability for vibration isolation. Yi et al. [34] achieved a novel kind of multi-resonant metamaterial by using piezoelectric materials and digital circuits, within which delicately designed control algorithms are implemented. While these efforts are helpful in broadening the target bandgap, the LR bandgap is relatively narrow and fixed [35]. Additionally, most of the multiple resonators enlarge the bandgap at the cost of added mass, which is unfavorable for practical applications that require broad bandgap and lightweight designs.

Compared to linear configurations, nonlinearities in engineering systems were once mainly viewed as dangerous due to their tendency to cause unwanted phenomena [36], such as chaos [37], secondary resonances [38], bifurcations [39], and abrupt discontinuous changes in vibration amplitude [40]. However, in the new millennium, and especially in its last decade, there has been a significant shift in the paradigm of nonlinear dynamics. The nonlinear dynamics community has started to exploit nonlinearities to achieve positive effects [41, 42]. This has also provided metamaterials with greater design freedom to reveal additional and interesting wave propagation phenomena and to pave the way for new approaches to manipulate bandgap for broadband applications. Nonlinearity enables a variety of wave responses in metamaterial media that are impossible to achieve with linear assumptions, such as resonance shift [43, 44], dispersion modulation [45, 46], sub- and super-harmonic resonances [47, 48], chaotic motion [49], non-reciprocal wave propagation [50, 51], and solitary waves [52, 53].

In the development of a nonlinear metamaterial, two types of nonlinear behavior, hardening or softening nonlinear types, are primarily considered. For a single nonlinear type, Narisetti et al. [46] used perturbation techniques to solve analytically the shifts of band structure for a weakly nonlinear hardening or softening monoatomic chain. Manktelow et al. [54] studied similar systems and documented wave-wave interactions with multiple scales approach. Lazarov et al. [55] studied amplitude-dependent dispersion and the shift of bandgap on a linear spring chain with attached Duffing-type cubic hardening nonlinear resonators using a harmonic balance method. Lepidi et al. [56] used an asymptotic approach to determine the dispersion properties separately for non-resonant lattices and for superharmonical 3:1 resonant lattices in a one-dimensional diatomic lattice with hardening nonlinear inter-atomic coupling. Additionally, Lepidi et al. [57] considered a one-dimensional mass-in-mass lattice with both geometric and constitutive nonlinearities in the internal resonator and pointed out the possibility of tailoring the properties to make the nonlinear waves faster in a hardening case or slower in a softening case. Xu et al. [58] combined the effects of hardening nonlinearity and damping on the band structure to achieve the broadband attenuation of elastic waves. Oh et al. [59] proposed a geometric softening nonlinearity-based NLM with a tunable bandgap at an extremely low frequency. Moreover, Xia et al. [60] focused on the bistable resonators in a linear spring chain and presented a qualitative demonstration of amplitude-dependent bandwidth enhancement. Subsequently, Xia et al. [61] replaced the linear spring chain with a continuous beam and presented experimental validations for nonlinear broadband attenuation. Furthermore, researchers considered strong nonlinear effects. Silva et al. [62] reported a half subharmonic attenuation zone in addition to the one around the fundamental frequency, which was

verified experimentally [63]. Fang et al. [49, 64] showed that ultra-broad bandgaps can be obtained from hardening nonlinear metamaterials by introducing a chaotic mechanism. Meanwhile, researchers have explored the potential of nonlinear metamaterials to achieve broadband attenuation through optimization [65–67]. Wu et al. [65] proposed a parametric optimization strategy for distributing multiple local resonances, aiming at achieving broadband nonlinear wave suppression. Shen et al. [66] studied a 1D metamaterial beam with embedded nonlinear resonators and investigated the nonlinear bandgap size variations with respect to the resonators nonlinearity via a multi-variable optimization. Shen et al. [67] further considered a 2D metamaterial honeycombs by embedding spider web-like nonlinear resonators and provided guidance on an optimization approach to further enlarge the bandgap size. These efforts have demonstrated that nonlinearity is an attractive design perspective for metamaterials. However, most studies of NLMs are limited to a single type of nonlinearity, either hardening nonlinearity or softening nonlinearity. A few studies are related to the combination of linear-plus-hardening nonlinear type [68, 69]. Consequently, the effects on the dispersion of the combination of linearity, hardening nonlinearity, and softening nonlinear types have not been well understood yet. Particularly, for the combined nonlinearity type, the quantitative evolution on the coupling effects on the dispersion curves and the underlying physical mechanisms remain largely unclear. Therefore, this study investigates three important aspects of the coupling effects. The first is to reveal how the combination of hardening and softening nonlinearity affects the shapes of the metamaterial's dispersion curves and leads to extremely enlarged bandwidth, which is more than twice of that of the linear case. The second is to reveal the physical mechanisms behind the dispersion regulation induced by the combinational nonlinearity. The last is the observation of the "dual wavevector" phenomenon, which offers new insights into the wave propagation control.

The main focus of this study is the mechanical model of a metastructure consisting of a basic unit with three resonators, two of which are situated within the host mass and may exhibit nonlinearity in the combination of linearity, hardening or softening. We explore the ultra-broad bandgap resulting from the combination of hardening and softening nonlinearity and investigate its physical origins by analyzing the nonlinear frequency responses of a single unit cell. The paper is structured as follows: Section 2 presents the mechanical and mathematical models, with the Lindstedt–Poincaré perturbation method used to derive the nonlinear dispersion relation of the governing equations. In Sect. 3, we explore the nonlinearity-induced bandgap resulting from hardening and softening nonlinearities, examining four combinations of stiffness properties of the primary and secondary internal springs and their effects on dispersion curves: hardening-plus-linear, linear-plus-hardening, softening-plus-linear, and linear-plus-softening. We also consider scenarios where the primary and secondary internal springs exhibit hardening and softening nonlinearity, respectively. Additionally, we investigate the transmission characteristics within the nonlinearity-induced bandgap. Numerical validations of the findings are presented in Sect. 4, and the conclusions are summarized in Sect. 5.

2 System description and mathematical modeling

The proposed nonlinear metastructure can be represented by a one-dimensional (1D) mass-in-mass chain, which contains periodic unit cells with a triplet of resonators, as shown in Fig. 1. Each unit cell consists of a discrete mass m_1 which is connected to the adjacent mass via a linear spring k_1. Inside each unit cell, there are two nonlinear Duffing resonators with different mass $m_i (i = 2, 3)$ and different spring coefficients (k_i, Γ_i), where k_i and Γ_i are the linear and nonlinear spring coefficients, respectively. The nonlinear force–displacement relationship of the Duffing resonator is given by $F_i = k_i x_i + \Gamma_i x_i^3$, where x_i is the deformation of the corresponding spring. Here, we only consider weak nonlinearity in the system and therefore adopt a perturbation approach to solve the corresponding governing equations. Hence, a perturbation parameter ε is introduced to express the nonlinear force–displacement relationship as $F_i = k_i x_i + \varepsilon \Gamma_i x_i^3$. For the nth cell, the governing equations can be expressed as:

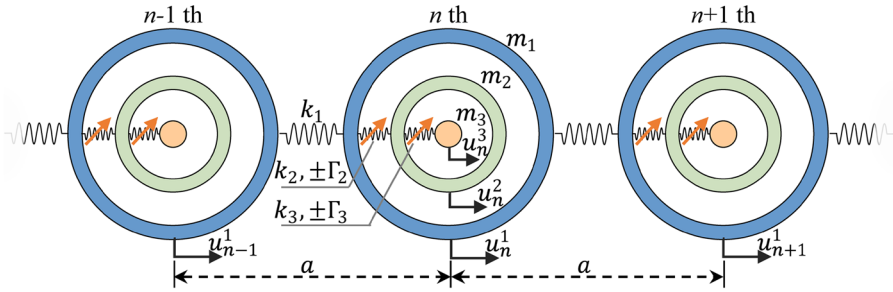

Fig. 1 Periodic mass-in-mass lattice whose units contain a triplet of resonators, two of which are placed inside the host mass and inside each other, both containing nonlinear springs

$$m_1\ddot{u}_1^n + k_1\left(2u_1^n - u_1^{n+1} - u_1^{n-1}\right) + k_2\left(u_1^n - u_2^n\right) + \varepsilon\Gamma_2\left(u_1^n - u_2^n\right)^3 = 0 \tag{1.1}$$

$$m_2\ddot{u}_2^n + \mathrm{k}_2\left(u_2^n - u_1^n\right) + \varepsilon\Gamma_2\left(u_2^n - u_1^n\right)^3 + k_3\left(u_2^n - u_3^n\right) + \varepsilon\Gamma_3\left(u_2^n - u_3^n\right)^3 = 0 \tag{1.2}$$

$$m_3\ddot{u}_3^n + k_3\left(u_3^n - u_2^n\right) + \varepsilon\Gamma_3\left(u_3^n - u_2^n\right)^3 = 0 \tag{1.3}$$

Non-dimensional parameters are introduced for the following analysis: $\theta_2 = \frac{m_2}{m_1}$ and $\theta_3 = \frac{m_3}{m_1}$ are the mass ratios; $\delta_2 = \frac{k_2}{k_1}$ and $\delta_3 = \frac{k_3}{k_1}$ are the linear stiffness ratios; $\gamma_2 = \frac{\Gamma_2}{k_1}$ and $\gamma_3 = \frac{\Gamma_3}{k_1}$ are the nonlinear stiffness ratios; $\tau = \omega t$ and $\Omega = \frac{\omega}{\omega_0}$ are the non-dimensional time and frequency, respectively, where $\omega_0 = \sqrt{\frac{k_1}{m_1}}$. By introducing these parameters, Eq. (1) can be rewritten as:

$$\Omega^2\frac{d^2u_1^n}{d\tau^2} + \left(2u_1^n - u_1^{n+1} - u_1^{n-1}\right) + \delta_2\left(u_1^n - u_2^n\right) + \varepsilon\gamma_2\left(u_1^n - u_2^n\right)^3 = 0 \tag{2.1}$$

$$\theta_2\Omega^2\frac{d^2u_2^n}{d\tau^2} + \delta_2\left(u_2^n - u_1^n\right) + \varepsilon\gamma_2\left(u_2^n - u_1^n\right)^3 + \delta_3\left(u_2^n - u_3^n\right) + \varepsilon\gamma_3\left(u_2^n - u_3^n\right)^3 = 0 \tag{2.2}$$

$$\theta_3\Omega^2\frac{d^2u_3^n}{d\tau^2} + \delta_3\left(u_3^n - u_2^n\right) + \varepsilon\gamma_3\left(u_3^n - u_2^n\right)^3 = 0 \tag{2.3}$$

The Lindstedt–Poincaré perturbation method [43] is then adopted to determine the dispersion relation of the nonlinear system. Due to the weak nonlinearity of the system, the higher-order terms, such as ε^2 or ε^3, are exceedingly small compared to ε^0 orε^1. Thus, the perturbation expansion of both frequency $\boldsymbol{\Omega}$ and displacement $u_j^n(j = 1, 2, 3)$ can be truncated to the first order as

$$\Omega = \Omega_0 + \varepsilon\Omega_1 \tag{3.1}$$

$$u_j = u_j^{n(0)} + \varepsilon u_j^{n(1)} \tag{3.2}$$

By substituting Eq. (3) into Eq. (2), independent equations for ε^0 and ε^1 terms can be separately considered as

$$\varepsilon^0 : \Omega_0^2\frac{\mathrm{d}^2u_1^{n(0)}}{\mathrm{d}\tau^2} + \left(2u_1^{n(0)} - u_1^{n+1(0)} - u_1^{n-1(0)}\right) + \delta_2\left(u_1^{n(0)} - u_2^{n(0)}\right) = 0 \tag{4.1}$$

$$\theta_2\Omega_0^2\frac{\mathrm{d}^2u_2^{n(0)}}{\mathrm{d}\tau^2} + \delta_2\left(u_2^{n(0)} - u_1^{n(0)}\right) + \delta_3\left(u_2^{n(0)} - u_3^{n(0)}\right) = 0 \tag{4.2}$$

$$\theta_3\Omega_0^2\frac{\mathrm{d}^2u_3^{n(0)}}{\mathrm{d}\tau^2} + \delta_3\left(u_3^{n(0)} - u_2^{n(0)}\right) = 0 \tag{4.3}$$

$$\varepsilon^1 : \Omega_0^2\frac{\mathrm{d}^2u_1^{n(1)}}{\mathrm{d}\tau^2} + \left(2u_1^{n(1)} - u_1^{n+1(1)} - u_1^{n-1(1)}\right) + \delta_2\left(u_1^{n(1)} - u_2^{n(1)}\right) = -2\Omega_0\Omega_1\frac{\mathrm{d}^2u_1^{n(0)}}{\mathrm{d}\tau^2} - \gamma_2\left(u_1^{n(0)} - u_2^{n(0)}\right)^3 \tag{5.1}$$

$$\theta_2\Omega_0^2\frac{\mathrm{d}^2u_2^{n(1)}}{\mathrm{d}\tau^2}+\delta_2\left(u_2^{n(1)}-u_1^{n(1)}\right)+\delta_3\left(u_2^{n(1)}-u_3^{n(1)}\right)=-2\theta_2\Omega_0\Omega_1\frac{\mathrm{d}^2u_2^{n(0)}}{\mathrm{d}\tau^2}-\gamma_2\left(u_2^{n(0)}-u_1^{n(0)}\right)^3-\gamma_3\left(u_2^{n(0)}-u_3^{n(0)}\right)^3 \tag{5.2}$$

$$\theta_3\Omega_0^2\frac{\mathrm{d}^2u_3^{n(1)}}{\mathrm{d}\tau^2}+\delta_3\left(u_3^{n(1)}-u_2^{n(1)}\right)=-2\theta_3\Omega_0\Omega_1\frac{\mathrm{d}^2u_3^{n(0)}}{\mathrm{d}\tau^2}-\gamma_3\left(u_3^{n(0)}-u_2^{n(0)}\right)^3 \tag{5.3}$$

The zeroth-order equations recover the governing equations of the corresponding LM. Therefore, the perturbation techniques are commonly utilized to transform nonlinear field equations into a hierarchy of linear equations, enabling the application of Floquet–Bloch conditions to nonlinear periodic systems. The first-order expansions can be recognized as a heterogeneous form of the linear system with the nonlinear terms acting as the forcing function. The frequency correction for each order of nonlinearity is then obtained by enforcing the requirement of non-secular solutions.

Considering Eq. (4), its harmonic solution can be assumed as:

$$u_j^{n(0)}=\frac{A_j^0}{2}e^{in\kappa}e^{i\tau}+c.c(j=1,2,3) \tag{6}$$

where $i=\sqrt{-1}$, $\kappa=qa$ denotes the dimensionless wave number, q represents the wave number, a is the lattice constant, $c.c$ refers to the complex conjugate, A_j^0 is the amplitude. By substituting Eq. (6) into Eq. (4) and applying the Floquet–Bloch conditions, in accordance with the reference [70], the linear dispersion equation can be obtained as

$$\begin{vmatrix}-\Omega_0^2+2[1-\cos(\kappa)]+\delta_2 & -\delta_2 & 0\\ -\delta_2 & -\theta_2\Omega_0^2+\delta_2+\delta_3 & -\delta_3\\ 0 & -\delta_3 & -\theta_3\Omega_0^2+\delta_3\end{vmatrix}=0 \tag{7}$$

By calculating the determinant, Eq. 7 can be rewritten as:

$$f(\kappa,\Omega_0)=a_1\Omega_0^6+a_2\Omega_0^4+a_3\Omega_0^2+a_4=0 \tag{8}$$

where

$$a_1=\theta_2\theta_3 \tag{9.1}$$

$$a_2=-(\delta_3\theta_2+\delta_2\theta_3+\delta_3\theta_3+2\theta_2\theta_3-2\cos(\kappa)\theta_2\theta_3+\delta_2\theta_2\theta_3) \tag{9.2}$$

$$a_3=-(-\delta_2\delta_3-2\delta_3\theta_2+2\cos(\kappa)\delta_3\theta_2-\delta_2\delta_3\theta_2-2\delta_2\theta_3+2\cos(\kappa)\delta_2\theta_3-2\delta_3\theta_3+2\cos(\kappa)\delta_3\theta_3-\delta_2\delta_3\theta_3) \tag{9.3}$$

$$a_4=-(2\delta_2\delta_3-2\cos(\kappa)\delta_2\delta_3) \tag{9.4}$$

As widely investigation in [70], three branches of frequency Ω_0 can be obtained for a given dimensionless wave number κ. Since the real wave number κ in Eq. (8) indicates passband, the bandgap condition for the zeroth order can be summarized as

$$\text{Passband if } 0\le\Omega_0\le\Omega_L^1 \text{ or } \Omega_U^1\le\Omega_0\le\Omega_L^2 \text{ or } \Omega_U^2\le\Omega_0\le\Omega_c \tag{10.1}$$

$$\text{First stop band if } \Omega_L^1\le\Omega_0\le\Omega_U^1, \text{second stop band } \Omega_L^2\le\Omega_0\le\Omega_U^2 \tag{10.2}$$

where Ω_L^1, Ω_U^1 and Ω_L^2, Ω_U^2 stand for the lower and upper edge frequencies of the first and second bandgaps, respectively, while Ω_c is the cut-off frequency.

By rearranging the zeroth-order equations, the following equations can be achieved

$$u_2^{n(0)}=\lambda u_1^{n(0)} \tag{11.1}$$

$$u_3^{n(0)}=\mu\lambda u_1^{n(0)} \tag{11.2}$$

where $\lambda=\frac{2[1-\cos(\kappa)]+\delta_2-\Omega_0{}^2}{\delta_2}$, $\mu=\frac{\delta_3}{\delta_3-\theta_3\Omega_0{}^2}$. Inserting Eq. (6) and Eq. (11) into Eq. (5), the first-order equations can be rewritten as:

$$(\chi_3\chi_2-\delta_3^2)\left[\Omega_0^2\frac{\mathrm{d}^2u_1^{n(1)}}{\mathrm{d}\tau^2}+\left(2u_1^{n(1)}-u_1^{n+1(1)}-u_1^{n-1(1)}\right)+\delta_2u_1^{n(1)}\right]-\chi_3\delta_2^2u_1^{n(1)}=c_1e^{in\kappa}e^{i\tau}+c_3e^{3in\kappa}e^{3i\tau}+c.c \tag{12.1}$$

$$\chi_2 u_2^{n(1)} = \delta_2 u_1^{n(1)} + \delta_3 u_3^{n(1)} - 2\theta_2\Omega_0\Omega_1 \frac{\mathrm{d}^2 u_2^{n(1)}}{\mathrm{d}\tau^2} - \gamma_2\left(u_2^{n(0)} - u_1^{n(0)}\right)^3 - \gamma_3\left(u_2^{n(0)} - u_3^{n(0)}\right)^3 \tag{12.2}$$

$$\chi_3 u_3^{n(1)} = \delta_3 u_2^{n(1)} - 2\theta_3\Omega_0\Omega_1 \frac{\mathrm{d}^2 u_3^{n(0)}}{\mathrm{d}\tau^2} - \gamma_3\left(u_3^{n(0)} - u_2^{n(0)}\right)^3 \tag{12.3}$$

where

$$\chi_2 = \theta_2\Omega_0^2 \frac{\mathrm{d}^2}{\mathrm{d}\tau^2} + \delta_2 + \delta_3 \tag{13.1}$$

$$\chi_3 = \theta_3\Omega_0^2 \frac{d^2}{d\tau^2} + \delta_3 \tag{13.2}$$

$$\begin{aligned} c_1 =& \frac{A_1^0}{2}\left[2\delta_2\delta_3\theta_3\mu\lambda + 2\delta_2\left(\delta_3 - \theta_3\Omega_0^2\right)\theta_2\lambda + 2\left(\left(\delta_3 - \theta_3\Omega_0^2\right)\right.\right. \\ & \left.\left(\delta_2 + \delta_3 - \theta_2\Omega_0^2\right) - \delta_3^2\right)\Big]\Omega_0\Omega_1 \\ & + \frac{A_1^0}{2}\left[\delta_2\delta_3\gamma_3(\lambda - \mu\lambda)^3\frac{3}{4}A_1^0\overline{A_1^0} - \delta_2\left(\delta_3 - \theta_3\Omega_0^2\right)\right. \\ & \left(\gamma_2(\lambda - 1)^3\frac{3}{4}A_1^0\overline{A_1^0} + \gamma_3(\lambda - \mu\lambda)^3\frac{3}{4}A_1^0\overline{A_1^0}\right) \\ & \left.-\left(\left(\delta_3 - \theta_3\Omega_0^2\right)\left(\delta_2 + \delta_3 - \theta_2\Omega_0^2\right) - \delta_3^2\right)\left(\gamma_2(1 - \lambda)^3\frac{3}{4}A_1^0\overline{A_1^0}\right)\right] \end{aligned} \tag{14}$$

where $\overline{A_1^0}$ is the conjugate amplitude of A_1^0. It is then noted that the force terms with functional form $e^{in\kappa}$ are secular terms that would lead to unbounded solutions. Thus, these terms must be eliminated. Subsequently, by solving the condition $c_1 = 0$ and separating Ω_0 and Ω_1, we obtain the explicit functional form of Ω_1 as

$$\begin{aligned} \Omega_1 =& f\left(\Omega_0, \gamma_2\left|A_1^0\right|^2, \gamma_3\left|A_1^0\right|^2\right) \\ =& 3/4\left|A_1^0\right|^2\Omega_0^7\left[\gamma_3\delta_2^2\theta_3^4 + \gamma_2\left(\delta_3(\theta_2 + \theta_3) - \theta_2\theta_3\Omega_0^2\right)^4\right] \\ & /\left[2\left(-\delta_3(\theta_2 + \theta_3)\Omega_0^2 + \theta_2\theta_3\Omega_0^4 + \delta_2\left(\delta_3 - \theta_3\Omega_0^2\right)\right)^2\right. \\ & \left(-2\delta_2\Omega_0^2\left(\delta_3 - \theta_3\Omega_0^2\right)\left(\delta_3(\theta_2 + \theta_3) - \theta_2\theta_3\Omega_0^2\right) + \Omega_0^4\right. \\ & \left.\left(\delta_3(\theta_2 + \theta_3) - \theta_2\theta_3\Omega_0^2\right)^2\right) \\ & + \delta_2^2\left(\delta_3^2(1 + \theta_2 + \theta_3) - 2\delta_3(1 + \theta_2)\theta_3\Omega_0^2 + (1 + \theta_2)\theta_3^2\Omega_0^4\right)\Big] \end{aligned} \tag{15}$$

According to Eqs. (3), (8), (15), the nonlinear dispersion relation can be finally expressed as

$$\Omega = \Omega_0 + \varepsilon f\left(\Omega_0, \gamma_2\left|A_1^0\right|^2, \gamma_3\left|A_1^0\right|^2\right) \tag{16}$$

where the dispersion relation for the linear case can be recovered by setting $\gamma_2, \gamma_3 = 0$.

3 Nonlinearity-induced bandgap for hardening and softening nonlinearities

From the nonlinear dispersion relation in Eq. (14), it is noted that both the nonlinear stiffness ratios (γ_2, γ_3) and the amplitude A_1^0 play important roles in band structure formation. We first investigated the effects of the nonlinear stiffness ratios by assigning six combinations of primary and secondary internal springs to the metamaterial unit cell, as shown in Table 1. The nonlinearity-dependent dispersion curves were calculated with different amplitudes. For simplicity, the following system parameters were selected: $[m_1\, m_2\, m_3\, k_1\, k_2\, k_3\, \varepsilon] = \left[1\ 1\ 1\ 1\ 1.5\ 1\ 1\ \times 10^3\right]$.

Table 1 Combinations of primary and secondary internal springs

Type	Primary internal spring		Secondary internal spring	
NLM1	$\gamma_2 = 1 \times 10^3$	(Hardening)	$\gamma_3 = 0$	(Linear)
NLM2	$\gamma_2 = 0$	(Linear)	$\gamma_3 = 1 \times 10^3$	(Hardening)
NLM3	$\gamma_2 = -1 \times 10^3$	(Softening)	$\gamma_3 = 0$	(Linear)
NLM4	$\gamma_2 = 0$	(Linear)	$\gamma_3 = -1 \times 10^3$	(Softening)
NLM5	$\gamma_2 = 1 \times 10^3$	(Hardening)	$\gamma_3 = -0.4 \times 10^3$	(Softening)
NLM6	$\gamma_2 = -0.4 \times 10^3$	(Softening)	$\gamma_3 = 1 \times 10^3$	(Hardening)

3.1 Hardening nonlinearity-induced bandgap

For Type NLM1, we plotted the dispersion curves in Fig. 2a. Here, the shaded areas represent the bandgap region of the corresponding linear case. First, by comparing the nonlinear case (solid line with circles/triangles) with the linear case (solid line with squares), it can be found that only the first and third branches of the band structure shift up. Such shifting is also reflected in the function mapping of Ω to Ω_0 obtained via Eqs. (15–16), as shown in Fig. 2b. Second, it can be found from Fig. 2a that the shifting up of the third branch is more apparent than that of the first branch, indicating an enlarged bandgap region, which is consistent with the shifting of the function mapping of Ω to Ω_0 in the first and third passband regions, as seen in Fig. 2b. Third, for both linear case and nonlinear case with small amplitude ($|A_1^0|^2 = 0.1$), the second bandgap ends at a point $\kappa = 0$. However, in the case ($|A_1^0|^2 = 0.2$) depicted by the solid line with triangles in Fig. 2a, the upper edge of the second bandgap is not at the frequency point corresponding to $\kappa = 0$, but jumps to the frequency point where the minimum of the third branch appears. Interestingly, we can also find from Fig. 2b that there is a local minimum of the function mapping of Ω to Ω_0 in the third passband region of the larger amplitude ($|A_1^0|^2 = 0.2$), which coincides with the minimum of the third branch in Fig. 2a.

To further quantify the presented shifting of the band structure attributable to the amplitude changes of the incident wave, we investigate the bandgap edge frequencies as functions of amplitude. Attention is paid to the previously derived condition of the bandgap in Eq. (8) which is combined with Eq. (14) to obtain the bandgap edge frequencies for the corresponding nonlinear system. Figure 2c shows the bandgap edge frequencies of NLM1 with different amplitudes of the incident wave. The black solid lines and red solid lines stand for the lower edge frequencies

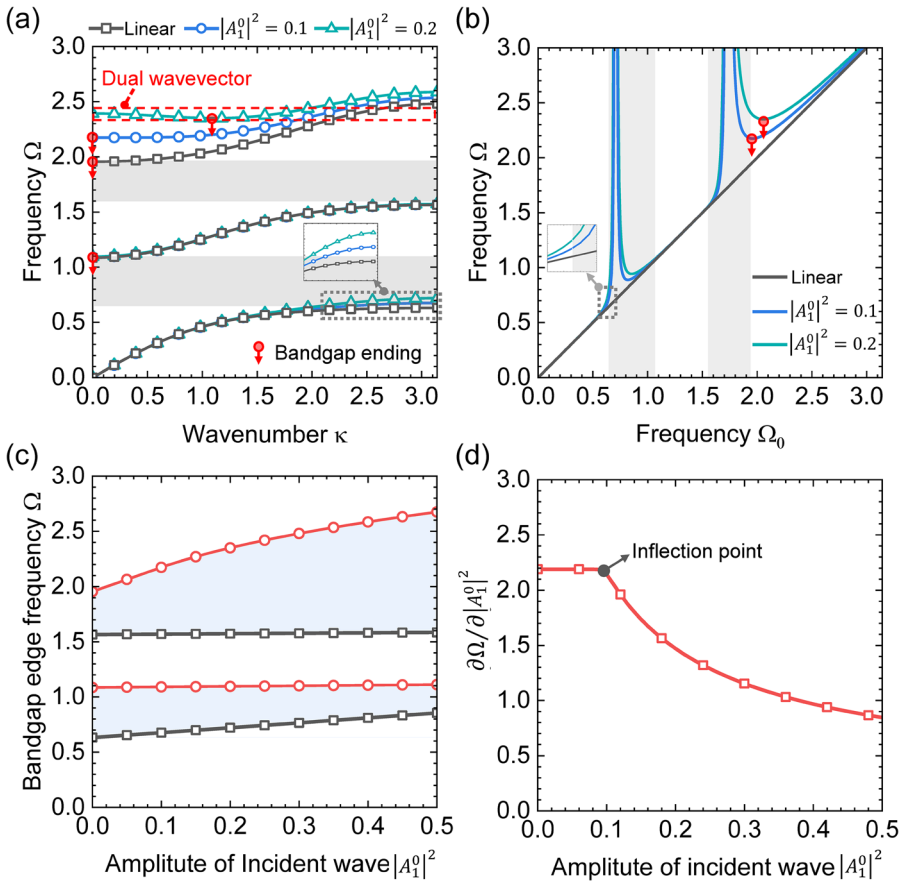

Fig. 2 Case NLM1: **a** dispersion curves; **b** function mapping of Ω to Ω_0; **c** Bandgap edge frequency variations with different amplitudes of the incident wave; **d** Derivative of the upper boundary of the second bandgap

and the upper edge frequencies, respectively. The shaded areas denote the bandgap regions. It is seen that when the amplitude increases, the first bandgap shrinks slightly, while the second bandgap expands apparently. In addition, the upper edge frequency of the first bandgap and the lower edge frequency of the second bandgap are unchanged, which implies that the effect of the incident wave's amplitude on the second passband branch is almost negligible. Figure 2d shows the derivative of the upper boundary of the second bandgap. It is important to mention that there is an inflection point at $\left|A_1^0\right|^2 = 0.1$. Such an inflection point corresponds to the jump mentioned above at the ending frequency point of the second bandgap from $\kappa = 0$ to the local minimum of the third branch. Furthermore, due to the ending frequency point's shifting of the second bandgap to the local minimum of the third branch, the third branch demonstrates a non-monotonic shape. It indicates that the wavevector κ as a function of frequency Ω is dual-valued. Such a "dual wavevector" region promises complicated nonlinear wave–wave interactions.

For Type NLM2, we plotted the dispersion curves in Fig. 3a. Unlike the results of Type NLM1, the shifting up of the second branch, which attributes to the amplitude change of the incident wave, is more pronounced than those of the first and third branches. Such shifting results in a dramatic narrowing and even vanishing of the second bandgap. Figure 3b shows the bandgap edge frequencies of Type NLM2 with different amplitudes of the incident wave. It can be found that the second bandgap vanishes when the amplitude $\left|A_1^0\right|^2 \geq 0.1$, while the first bandgap only moves up to a higher-frequency region with a little change in width.

3.2 Softening nonlinearity-induced bandgap

For Type NLM3, we plotted the dispersion curves in Fig. 4a. The outcome is similar to that of Type NLM1 since the effect of nonlinearity on the band structure is dominant in the first and third branches. However, in contrast to the hardening nonlinearity, the softening nonlinearity causes the shifting down of the two branches, particularly the third branch. Such shifting also results in a dramatic narrowing and even vanishing of the second bandgap. It can be found that the second bandgap vanishes when the amplitude $\left|A_1^0\right|^2 \geq 0.18$, as shown in Fig. 4b.

For Type NLM4, we plotted the dispersion curves in Fig. 5a. First, it can be seen that the second branch shifts down far more significantly than the first and third branches. This can also be revealed in Fig. 5b, where the difference between the linear system and nonlinear system occurs more apparently in the second passband region. Second, the shifting down of the second branch is concentrated in a large wavenumber region, indicating an enlarged bandgap region. Third, the second bandgap starts at $\kappa = \pi$ for the linear case, as shown in Fig. 5a. However, in the case $\left|A_1^0\right|^2 = 0.1$

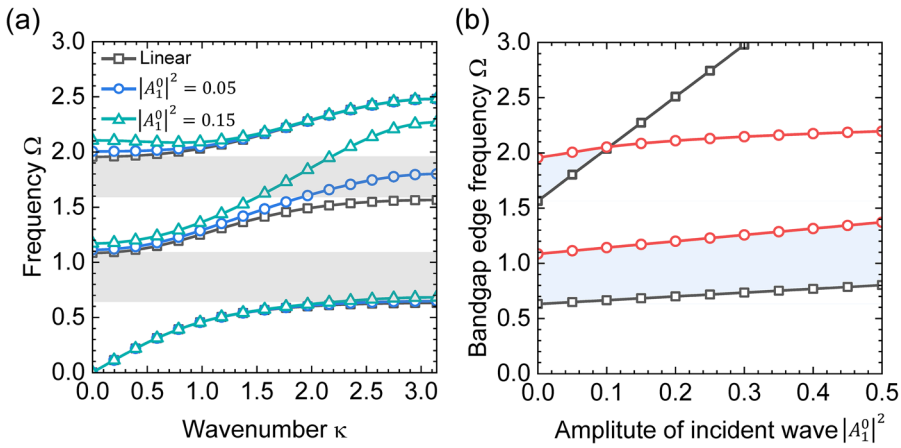

Fig. 3 Type NLM2: **a** Dispersion curves; **b** Bandgap edge frequency variations with different amplitudes of the incident wave

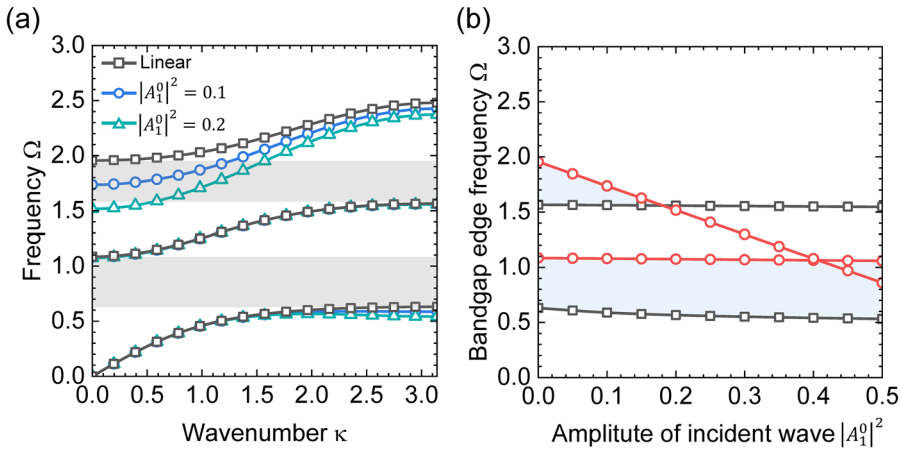

Fig. 4 Type NLM3: **a** Dispersion curves; **b** Bandgap edge frequency variations with different amplitudes of the incident wave

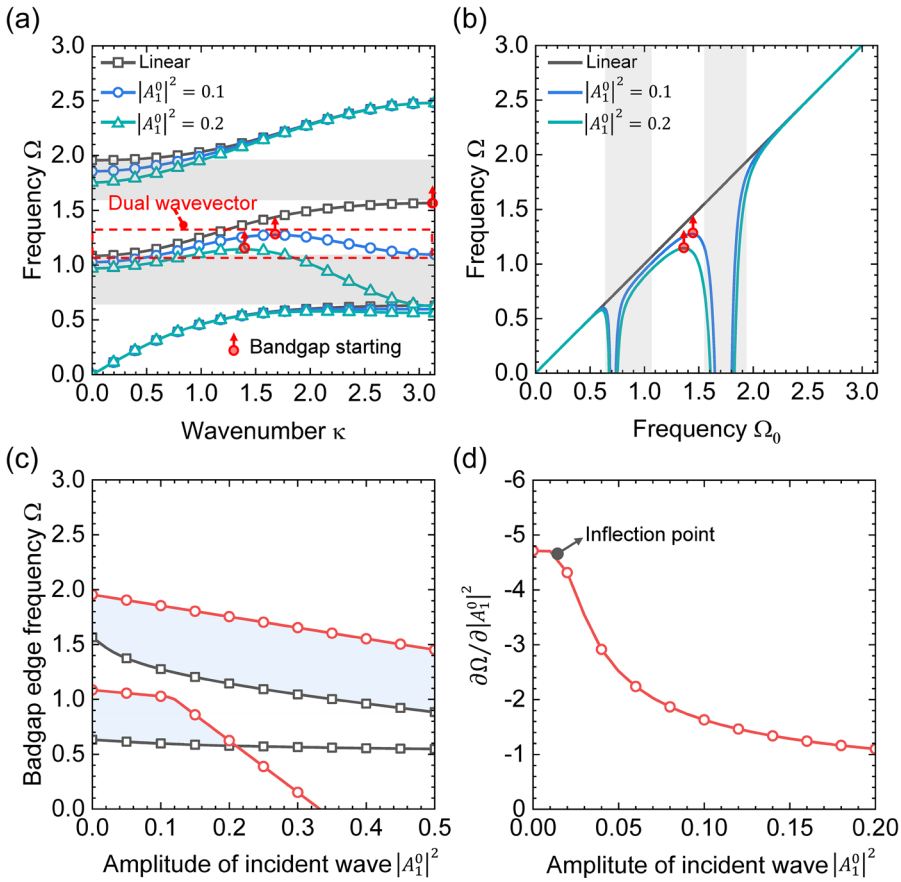

Fig. 5 Type NLM4: **a** Dispersion curves; **b** Function mapping of Ω to Ω_0; **c** Bandgap edge frequency variations with different amplitudes of the incident wave; **d** Derivative of the lower boundary of the second bandgap

and $|A_1^0|^2 = 0.2$, the starting frequency point of the second bandgap jumps to the frequency point where a local maximum of the second branch appears. Also, it can be seen from Fig. 5b that there is a local maximum of the function mapping of Ω to Ω_0 in the second passband region, which coincides with the local maximum of the second branch.

Furthermore, Fig. 5c shows the effect of the amplitude on the bandgap edge frequencies. It can be found that the shifting down of the second branch closes the first bandgap when the amplitude

$|A_1^0|^2 \geq 0.2$. Besides, there is also an inflection point at $|A_1^0|^2 = 0.01$ in the derivative of the lower boundary of the second bandgap, as shown in Fig. 5d. Such an inflection point also corresponds to the jump mentioned above of the starting frequency point of the second bandgap from $\kappa = \pi$ to the local maximum of the second branch. Finally, similar to Type NLM1, the "dual wavevector" phenomenon is also observed for the softening nonlinearity, as shown in the dashed box in Fig. 5a.

3.3 Hardening–softening nonlinearity-induced ultra-broad bandgap

The previous considerations of the four stiffness combinations only involve the cases where one spring is assigned as nonlinear. The results reveal that the effects of nonlinearity on the primary or secondary spring are dominant in the third branch or the second branch, respectively. It is worth remarking that the hardening nonlinearity of the primary spring or the softening nonlinearity of the secondary spring can widen the second bandgap region via shifting up the upper boundary or shifting down the lower boundary of the second bandgap, respectively.

The aroused question to answer is whether combining the hardening and softening nonlinearities can provide potential advancements in broadband vibration suppression and new wave propagation phenomena. Specifically, we seek to understand the quantitative evolution process of coupling effects of both hardening and softening on bandgap phenomena. To demonstrate these coupling effects, we consider two typical combinations. For Type NLM5, we assign the hardening nonlinearity ($\gamma_2 = 1\text{E}3$) to the primary spring and the softening nonlinearity ($\gamma_3 = -0.4\text{E}3$) to the secondary spring. The second combination, namely Type NLM6, has the opposite configuration to Type NLM5. Additionally, we also examine a mass-in-mass chain with one resonator, where the internal spring is considered as either with a hardening or softening nonlinearity.

Figure 6 presents a comparison of four investigated cases in dispersion curves. Firstly, for a mass-in-mass chain, its dispersion curves can be calculated by setting k_3 to an infinite value, in which case the model depicted in Fig. 1 degenerates into a mass-in-mass chain model. Figure 6a and b demonstrates that a single nonlinear resonator can only provide simple regulation to the dispersion curve. The upshift or downshift of dispersion curves is attributed to the presence of single-hardening or single-softening nonlinearity, respectively. Additionally, the results of dispersion curves show a good agreement with those obtained by the multiple-scale method [71], which also reflects that the calculation method in Sect. 1 is reliable and correct. Secondly, for Type NLM5, Fig. 6c illustrates the upshift of the third branch and

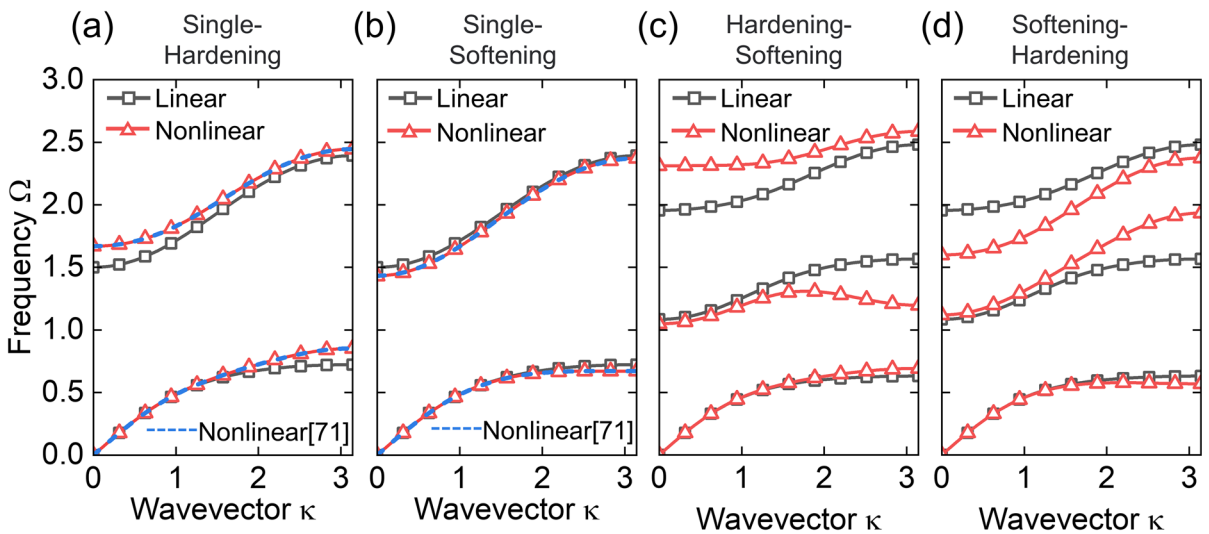

Fig. 6 The comparison of four investigated cases in dispersion curves. **a** Single-hardening nonlinearity and **b** single-softening in internal springs of mass-in-mass chain, respectively; **c**Type NLM5; **d** Type NLM6

the downshift of the second branch. Consequently, a notably widened bandgap forms between the non-dimensional frequencies $\Omega_L^{\mathrm{NLM},2} = 1.30$ and $\Omega_U^{\mathrm{NLM},2} = 2.31$. The bandgap of the NLM5 is observed to be widened by up to 252% when compared with the bandgap of LM between non-dimensional frequencies $\Omega_L^{\mathrm{LM},2} = 1.56$ and $\Omega_U^{\mathrm{LM},2} = 1.96$. It should be noted that the width of the first bandgap of Type NLM5 shrinks by 20% with respect to the linear case. Thirdly, for Type NLM6, as shown in Fig. 6d, the first and third branches shift down, while the second branch shifts up, which does not widen the bandgap.

In summary, the effects of nonlinearity on the shift of dispersion curves and bandgap depend not only on the type of nonlinearity but also on the location of the nonlinearity configuration. Therefore, the combined design of hardening and softening nonlinear provides a novel design framework that significantly enriches the design space and leads to substantial advancements in broadband vibration suppression.

As discussed in Fig. 6, the shift and the width change of the second bandgap is most sensitive to nonlinearity. As demonstrated earlier [70], the width of the second bandgap decreases with the increase of the stiffness ratio parameter k_3/k_2. For example, when k_3/k_2 approaches infinity, the second band gap eventually disappears. In such a case, the model depicted in Fig. 1 degenerates into the mass-in-mass chain with one resonator. Therefore, in order to fully showcase the advantages of combined nonlinearity in a regulating band structure, it is suggested to select the value of k_3 around the value of k_2.

To demonstrate the generality of the observed bandgap widening phenomenon under the combination of hardening and softening nonlinearities, we consider three cases of stiffness assignment: $k_2 > k_3$, $k_2 = k_3$, $k_2 < k_3$. Figure 7 compares the dispersion curves for linear and nonlinear cases in the above three stiffness assignment scenarios for the combination of hardening and softening nonlinearities. The bandgaps for linear and nonlinear are depicted in Fig. 7 as gray shaded areas and light red shaded areas, respectively. It is evident that the widening of the width of the second bandgap induced by nonlinearity is valid for all three stiffness assignments. In fact, the width of the second bandgap increases by up to more than twice as wide as those bandgaps in the corresponding LM, which are 252%, 248%, and 286% for the three stiffness assignment scenarios, respectively.

Furthermore, it is important to note that the dispersion curves of nonlinear metamaterials are not only influenced by the combination of the different nonlinear types but also by the strength of the nonlinearity. Therefore, we investigate the effects of

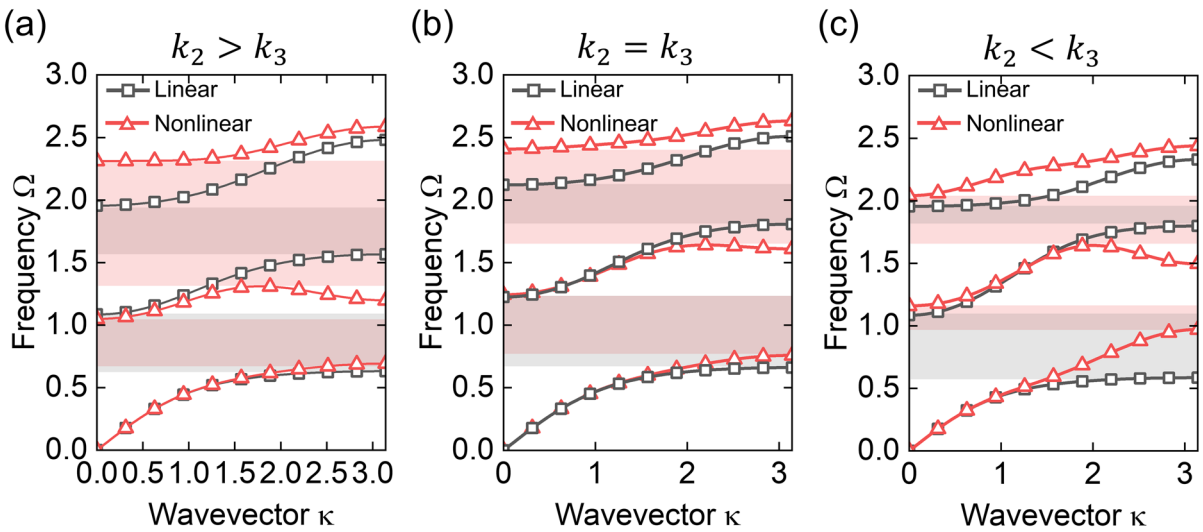

Fig. 7 Dispersion curves for the combination of hardening and softening nonlinearities, with three typical stiffness assignment cases: **a** $k_2 = 1.5 > k_3 = 1$, $\Omega_U^{\mathrm{NLM},2} = 2.31$, $\Omega_L^{\mathrm{NLM},2} = 1.3$, $\Omega_U^{\mathrm{LM},2} = 1.96$, $\Omega_L^{\mathrm{LM},2} = 1.56$; **b** $k_2 = k_3 = 1.5$, $\Omega_U^{\mathrm{NLM},2} = 2.41$, $\Omega_L^{\mathrm{NLM},2} = 1.64$, $\Omega_U^{\mathrm{LM},2} = 2.12$, $\Omega_L^{\mathrm{LM},2} = 1.81$; **c** $k_2 = 1 < k_3 = 1.5$, $\Omega_U^{\mathrm{NLM},2} = 2.10$, $\Omega_L^{\mathrm{NLM},2} = 1.64$, $\Omega_U^{\mathrm{LM},2} = 1.96$, $\Omega_L^{\mathrm{LM},2} = 1.80$;

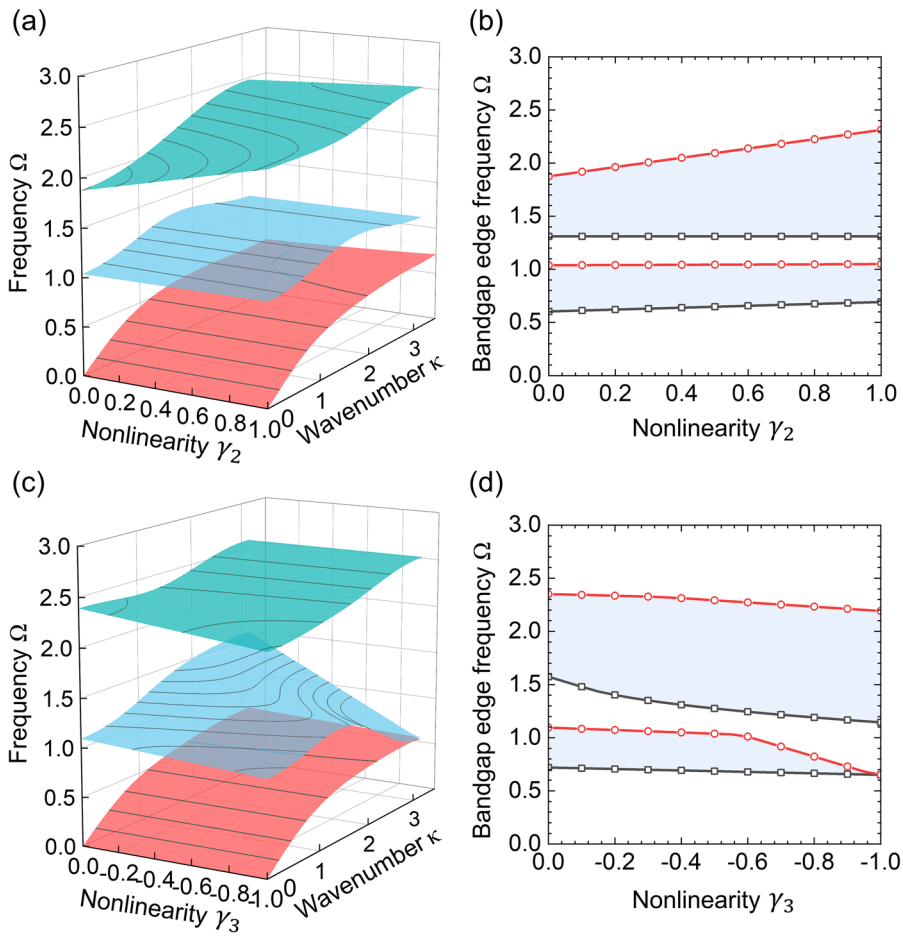

Fig. 8 The variation of dispersion curves and the corresponding bandgap edge frequency with the change of nonlinearity for the combination of hardening and softening nonlinearities. **a** and **b** The interval for γ_2 is [0, 1] and γ_3 remains constant at -0.4×10^3; (c) and (d) the interval for γ_2 remains constant at 1×10^3 and the interval for γ_3 is [0, − 1];

nonlinearity strength on the variation of dispersion curves and the bandgap edge frequency for the combination of hardening and softening nonlinearities.

Firstly, in Fig. 8a and b, when the nonlinear stiffness ratios γ_2 change from 0 to 1 and γ_3 remains constant at -0.4×10^3, it is observed that the lowest point of the third branch dispersion curve gradually shifts toward the high-frequency region as γ_2 increases. This shift indicates an upshift of the upper bound of the second bandgap. Additionally, as shown in Fig. 8b, the second band gap gradually widens as γ_2 increases. Moreover, the second branch dispersion curve remains unchanged as γ_2 increases. Secondly, as shown in Fig. 8c and d, when the nonlinear stiffness ratios γ_2 remain constant at 1×10^3 and γ_3 changes from 0 to -1, it is observed that the highest point of the second branch dispersion curve gradually shifts toward the low frequency as γ_2 changes from 0 to -1. This shift corresponds to a downshift of the lower bound of the second bandgap, as shown in Fig. 8d. Consequently, the second band gap also gradually widens as γ_3 changes from 0 to -1. It is also noteworthy that the lowest point of the second branch dispersion curve gradually encroaches upon the first bandgap as γ_2 changes from 0 to -1.

3.4 Transmission characteristics inside the amplitude-induced bandgap

To get an insight into the dynamics of the NLM with widened bandgap, wave transmission is studied analytically. For a finite linear periodic system containing n units, the transmission can be defined as:

$$T_l = \left|\prod_{n=1}^{n} T_n\right| = \left|\prod_{n=1}^{n} \frac{A_1^0 e^{i(\kappa n-\tau)}}{A_1^0 e^{i((\kappa(n-1))-\tau)}}\right| = \left|e^{i\kappa n}\right| \quad (17)$$

where A_1^0 is the amplitude of the initial wave. In the bandgap region, the transmission is less than 1 due to the imaginary value of κ. However, for a nonlinear periodic system, κ depends on the change in the amplitude. Thus, the transmission after n unit cells can be calculated by using a method of recurrence as:

$$T_{nl} = \prod_{n=1}^{n}\left|\frac{u_1^n}{u_1^{n-1}}\right| = \prod_{n=1}^{n}\left|e^{i\kappa\left(A_1^{n-1}\right)}\right| \quad (18)$$

where A_1^{n-1} are the wave amplitude at the n-th unit cell, while $\kappa\left(A_1^{n-1}\right)$ denotes the corresponding wavenumber as a function of the wave amplitude. To calculate $e^{i\kappa\left(A_1^{n-1}\right)}$, one can separate $\cos(\kappa)$ and Ω_0 from Eq. (8) and apply the Euler formula. Then, Eq. (8) is rewritten as:

$$\cos\left[\kappa\left(A_1^{n-1}\right)\right] = f(\Omega_0) = \frac{e^{i\kappa\left(A_1^{n-1}\right)} + e^{-i\kappa\left(A_1^{n-1}\right)}}{2} \quad (19)$$

where the detailed form of $f(\Omega_0)$ can be expressed as:

$$\begin{aligned} f(\Omega_0) =& 1 + \left[(\delta_2\delta_3 + \delta_2\delta_3\theta_2 + \delta_2\delta_3\theta_3)\Omega_0^2\right. \\ &+(-\delta_3\theta_2 - \delta_2\theta_3 - \delta_3\theta_3 - \delta_2\theta_2\theta_3)\Omega_0^4 + \theta_2\theta_3\Omega_0^6\left.\right] \\ &/\left[-2\delta_2\delta_3 + (2\delta_3\theta_2 + 2\delta_2\theta_3 + 2\delta_3\theta_3)\Omega_0^2 - 2\theta_2\theta_3\Omega_0^4\right] \end{aligned} \quad (20)$$

Multiplying $2e^{i\kappa\left(A_1^{n-1}\right)}$ on both sides of Eq. (19) and simplifying it, yields:

$$e^{2i\kappa\left(A_1^{n-1}\right)} - 2f(\Omega_0)e^{i\kappa\left(A_1^{n-1}\right)} + 1 = 0 \quad (21)$$

Solving Eq. (21) with respect to $e^{i\kappa\left(A_1^{n-1}\right)}$ yields:

$$e^{i\kappa\left(A_1^{n-1}\right)} = f(\Omega_0) \pm \sqrt[2]{f^2(\Omega_0) - 1} \quad (22)$$

Based on these equations, we can obtain the nonlinear transmission subsequently. First, for the amplitude A_1^0 and frequency Ω, $e^{i\kappa\left(A_1^0\right)}$ is calculated from Eq. (20), where Ω_0 is calculated from Eq. (16). Then, the amplitude after the 1st unit cell A_1^1 is calculated as $A_1^1 = A_1^0\left|e^{i\kappa\left(A_1^0\right)}\right|$. Finally, the process is repeated to calculate $\left|e^{i\kappa\left(A_1^{n-1}\right)}\right|$ and the nonlinear transmission can be obtained by Eq. (18). Figure 9 shows the transmission results calculated on a periodic chain with 20 unit cells of both the linear case and Type NLM5 with three levels of amplitude. For Type NLM5 with a small amplitude $\left|A_1^0\right|^2 = 0.02$, the corresponding transmission result is in good agreement with that of the linear case. The wave attenuation regions agree reasonably well with the predictions of the bandgaps in Fig. 6c. When the amplitude increases, one can observe an ultra-broad attenuation region of Type NLM5, which has two new wave attenuation regions on both sides of the original second bandgap region of the linear case (dark-pink

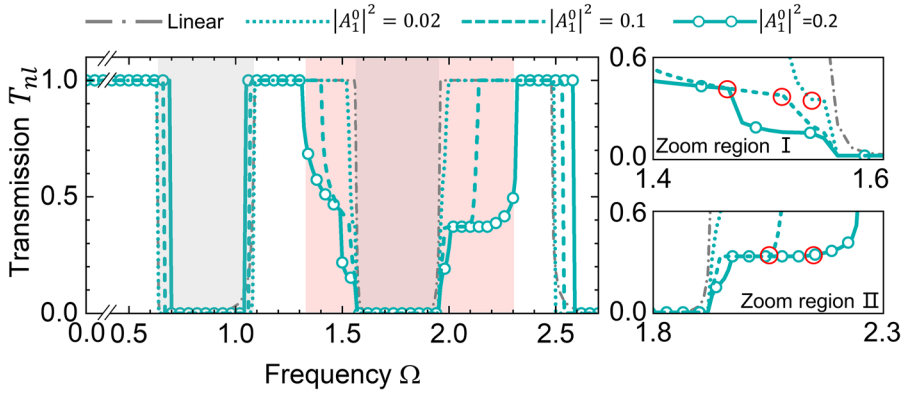

Fig.9 Transmission through the periodic chain with 20 unit cells for the linear case and Type NLM5 with three levels of amplitude. Dark-pink shaded area represents the bandgap region of the linear case, and light-pink shaded areas represent the bandgaps induced by nonlinearity

shaded area). For $\left|A_1^0\right|^2 = 0.2$, the boundary of the attenuation region is consistent with the prediction of the bandgap in Fig. 6c. Also, it is noteworthy that the transmissions for Type NLM5 change gradually, while the transmission for the linear case has a dramatic change. This behavior is understandable due to the amplitude dependency of the bandgap for NLM. When the frequency is closer to the edges of the bandgaps induced by nonlinearity (light-pink shaded areas), a larger amplitude is required to activate the nonlinear effect. If the amplitude is not sufficient to excite the nonlinear behavior, the bandgaps induced by nonlinearity can still permit wave propagation. As a result, the transmissions for Type NLM5 vary gradually between 0 and 1 in the corresponding nonlinearity-induced bandgap regions, as shown in Fig. 6c. Furthermore, we can see inflection points in the zoomed region I and zoomed region II, as illustrated in the enlarged parts of the transmission diagram given on the right-hand side of Fig. 9. This is supported by the properties of $\frac{\partial\Omega}{\partial A_1^0}$ mentioned earlier related to Figs. 2d and 5d.

4 Numerical validation

In this section, nonlinear dynamic responses of the unit cell and the wave propagation in a periodic chain of TYPE NLM5 were studied numerically. First, the physical origin of the nonlinearity-induced bandgap can be explained with the help of the nonlinear frequency responses analysis of a unit cell, as shown in Fig. 10a. A sinusoidal displacement of $u = A_1^0 \sin(\omega t)$ was applied to the left connection point of the linear spring. Here, $\left|A_1^0\right|^2 = 0.2$ is the same as Type NLM5 in Sect. 3.3. The third-order harmonic balance method was used to obtain the frequency responses of the unit cell with the help of an open-source package NLvib_v1.3 [72]. Figure 10b shows the comparison of the frequency responses of the unit cell for four different cases: linear case, hardening-plus-linear type with the parameters $\gamma_2 = 1\text{E}3$ and $\gamma_3 = 0$, linear-plus-softening type with the parameters $\gamma_2 = 0$ and $\gamma_3 = -0.4\text{E}3$, hardening-plus- softening type with the parameters same as type NLM5. The displacement transmission was defined as $T_{u1} = \log\left(\frac{A_{u1}}{A_1^0}\right)$. The amplitude A_{u1} was determined by the root mean square of the amplitude of $u_1(t)$ over 20 periods.

For the linear case, it can be found that there are three resonant modes and two attenuation regions (grey shaded areas). Here, the generation of the linear attenuation region can be simply explained with a vibration absorber. And the frequency range of the attenuation region is consistent with the bandgap region in Fig. 6c. Figure 10c and d shows the response obtained for $\frac{u_i}{A_1^0}(i = 1, 2, 3)$ at the frequency of positions A and B, respectively. The attenuation of u_1 is obvious. The motion of u_2 and u_3 is in phase at the frequency of position A and antiphase at B. It is also noted that the peak-to-peak amplitude of the secondary mass is higher than the primary one at A, while the opposite holds for B.

By comparing the frequency responses of u_1 for the linear and nonlinear systems, the following remarks can be made from Fig. 10b. First, the resonance peaks of the hardening system (blue dotted line) shift to higher frequencies, especially the third resonance peak. Also, a remarkable reduction of the amplitude in the shaded region II can be observed, which indicates that an attenuation region happens at the third resonant frequency region of the linear system. This explains why the hardening nonlinearity-induced bandgap appears in Fig. 2a. Second, distinguished from the hardening behavior, the resonance peaks of the softening system (green dashed line) shift to lower frequencies, especially the second resonance peak, which also causes an attenuation region I at the second resonant frequency region of the linear system. Such attenuation region is also in accordance with the appearance of the softening nonlinearity-induced bandgap seen in Fig. 5a. Finally, considering the joint effect of hardening and softening nonlinearity (red solid line), apparent attenuation regions I and II appear simultaneously on both sides of the original second bandgap of the linear system. This corresponds to the underlying mechanism that yields the ultra-broad bandgap in Fig. 6c for the hardening-plus-softening nonlinear system. It should be noted that the frequency–amplitude response curves plotted in Fig. 10b exhibit certain bending and loops at lower frequencies, and these phenomena have already been reported for nonlinear attachments [73, 74]. In addition, Fig. 10e and f indicates that the displacement u_1 of the hardening-plus-softening nonlinear system is

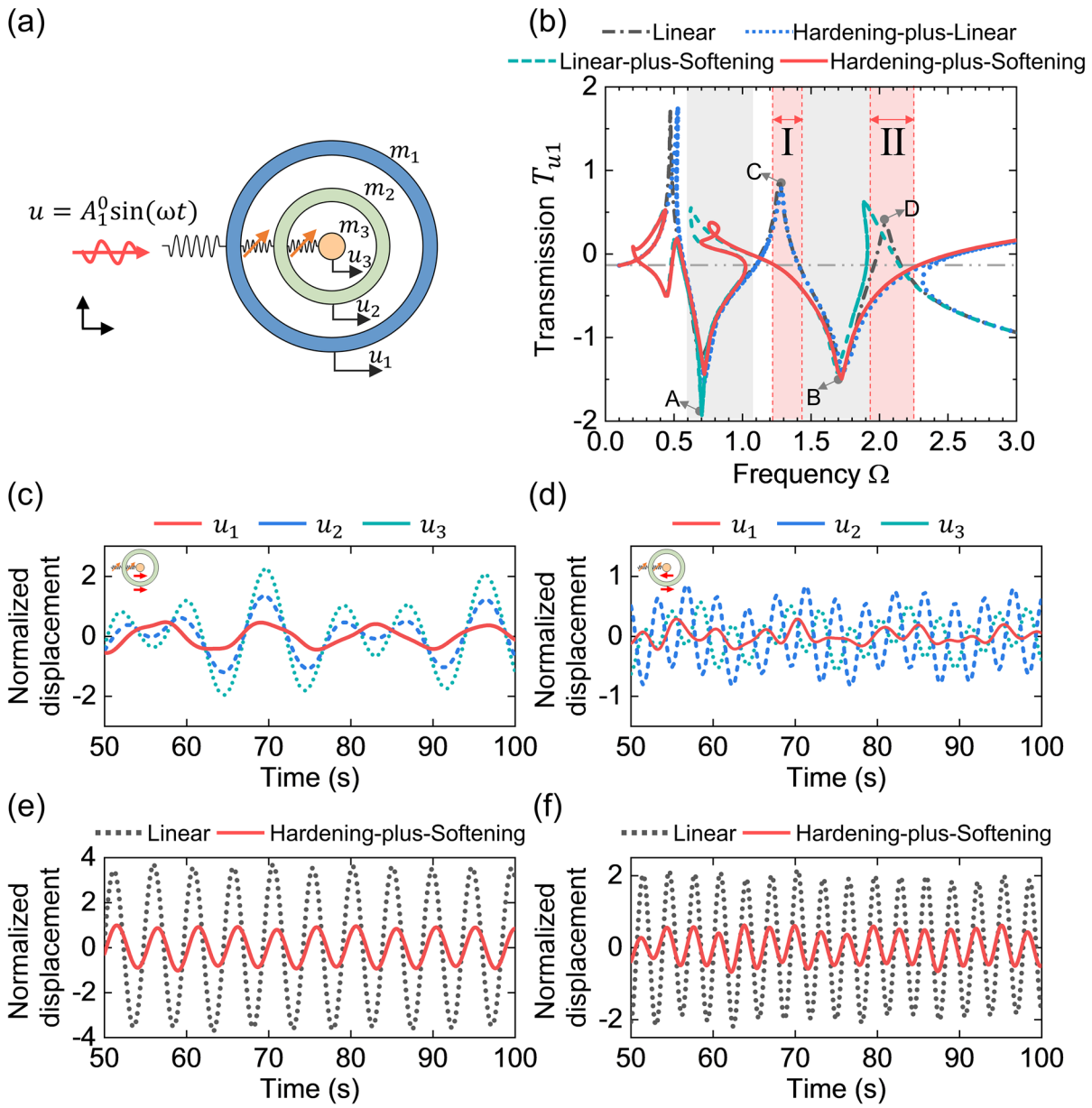

Fig.10 **a** Model of a unit cell; **b** Frequency responses curves; **c** and **d** Normalized displacements obtained at the frequency of position A and B labelled in (**b**); **e** and **f** Comparison of normalized displacement responses of u_1 between the hardening–softening nonlinear system and the linear system at the frequency of positions C and D

considerably smaller than that of the linear system at the frequency of positions C and D, respectively.

Wave propagation in a periodic chain consisting of 800 unit cells was also studied numerically, as shown in Fig. 11a. The numerical integration of Eq. (2) was carried out with the fourth-order Runge–Kutta method in MATLAB. Here, 800 unit cells are considered to successfully separate the reflected waves from the transmitted waves. A harmonic excitation was applied to the first unit cell. The excitation amplitude A_b is the same as Type NLM5 in Sect. 3.3. The displacement transmission was evaluated by $\left|\frac{A_{20}}{A_b}\right|$, where A_{20} is the root-mean-square (RMS) amplitude of the measured time transient displacements of the 20th unit cell averaged over 20 periods.

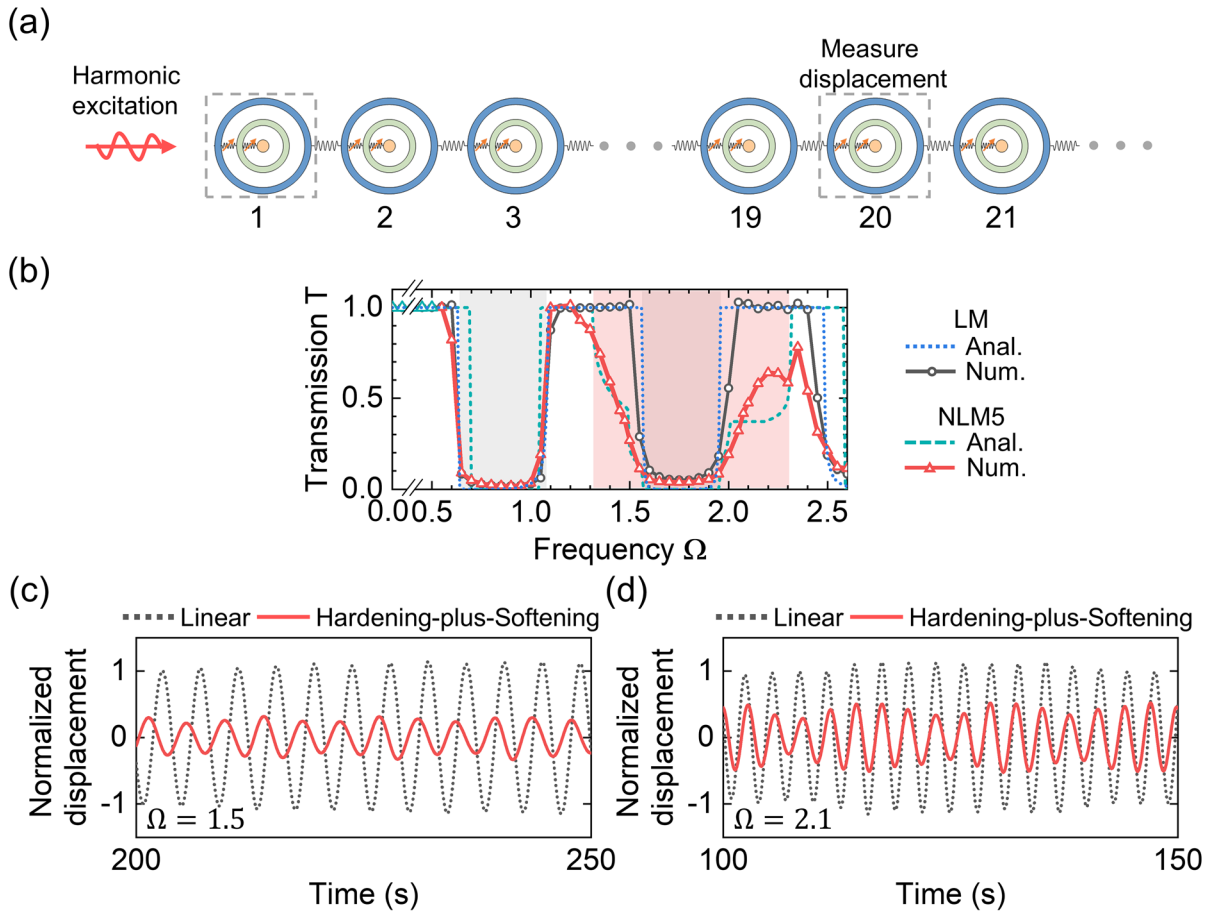

Fig.11 **a** Numerical simulation setting for the periodic chain to measure transmission; **b** comparison of displacement transmission between numerical and analytical results; **c** and **d** normalized displacement responses of u_1 in the time domain at $\Omega = 1.5$ and $\Omega = 2.1$

Figure 11b shows the comparison of displacement transmission between numerical and analytical results. Both the linear case and Type NLM5 were studied. For the linear case, the numerical and analytical transmission results are in good agreement. The wave attenuation frequency ranges are well predicted by the bandgap regions (grey shaded regions). Particularly, the existence of an ultra-broad second bandgap region, which is induced by nonlinearity, is numerically confirmed for Type NLM5. Figure 11c and d shows the time-domain displacement responses of u_1 at $\Omega = 1.5$ and $\Omega = 2.1$, respectively. Obvious attenuations can be found with respect to the results of the linear case. It should be added that there is a slight discrepancy between the analytical and numerical results in the first bandgap region for Type NLM5. This is because the wave amplitude decays in the original linear bandgap region, which prevents the nonlinear oscillations from being excited at a small excitation amplitude.

5 Conclusion

This work has been concerned with metastructures whose mechanical model corresponds to a one-dimensional mass-in-mass chain, which contains periodic unit cells with a triplet of resonators. A spring that connects the primary mass to the host mass and the other one that connects the secondary mass to the primary mass have been considered to be of different types, but always including nonlinearity: hardening-plus-linear, linear-plus-hardening, softening-plus-linear, linear-plus-softening, as well as hardening-plus-softening. For all these cases, of interest has been to obtain dispersion curves and bandgaps. To

obtain them, the governing equations have been created and solved by the Lindstedt–Poincaré method, treating the system as weakly nonlinear.

In the hardening-plus-linear case, the increase in the amplitude has been found to affect the first and third branches of the band structure. Shifting up of the third branch is more apparent in the long wavelength region, which means that the bandgap is widened. If the amplitude is larger than the critical amplitude ($|A_1^0|^2 = 0.1$), a boundary of the band gap appears at a point where the minimum of the third branch exists. The corresponding frequency range was denoted as the "dual wavevector" region.

For the case of linear-plus-hardening nonlinearity, shifting up of the second branch is most pronounced in the short wavelength region, resulting in the reduction of the second bandgap. The second bandgap closes to zero when the amplitude $|A_1^0|^2 \geq 0.1$.

In the softening-plus-linear case, the influence of nonlinearity on the band structure is dominant in the third branch, as in the hardening-plus-linear case. However, here, the softening nonlinearity causes the third branch to shift down, resulting in the shrink of the second bandgap. The second bandgap closes to zero when the excitation amplitude $|A_1^0|^2 \geq 0.18$.

For the linear-plus-softening case, the second branch is shifted down, and this shift is concentrated in the short wavelength region, widening the second bandgap. Shifting down of the second branch closes the first bandgap when this amplitude $|A_1^0|^2 \geq 0.2$.

It has been shown that in the hardening-plus-softening case, an ultra-broad bandgap appears above the fundamental one and its width is more than twice as wide as the bandgap in the corresponding linear case, which is a novel and significant extension. Future work involves practical realizations and experimental verification of this finding.

Acknowledgements This work was supported in part by the National Key Research and Development Program of China under Grant No. 2021YFE0110900 and in part by the National Natural Science Foundation of China (NSFC) under Grants No. U22B2078, 11991033 and 12202052. The involvement of Ivana Kovacic was supported by the Ministry of Science, Innovation and Technological Development of the Republic of Serbia via the NOLIMAST project.

Funding The authors list their funding sources in the Acknowledgements.

Data availability Relevant data can be made available upon reasonable request.

Declarations

Conflict of interest The authors declare that they have no conflict of interest.

References

1. Liu, Z., Zhang, X., Mao, Y., Zhu, Y.Y., Yang, Z., Chan, C.T., Sheng, P.: Locally resonant sonic materials. Science **289**, 1734–1736 (2000). https://doi.org/10.1126/science.289.5485.1734
2. Liu, Z., Chan, C.T., Sheng, P.: Analytic model of phononic crystals with local resonances. Phys. Rev. B–Condens. Matter Mater. Phys. **71**, 1–8 (2005). https://doi.org/10.1103/PhysRevB.71.014103
3. Liu, X.N., Hu, G.K., Huang, G.L., Sun, C.T.: An elastic metamaterial with simultaneously negative mass density and bulk modulus. Appl. Phys. Lett. **98**, 2–4 (2011). https://doi.org/10.1063/1.3597651
4. Zhu, R., Liu, X.N., Hu, G.K., Sun, C.T., Huang, G.L.: Negative refraction of elastic waves at the deep-subwavelength scale in a single-phase metamaterial. Nat. Commun. **5**, 1–8 (2014). https://doi.org/10.1038/ncomms6510
5. Scheibner, C., Souslov, A., Banerjee, D., Surówka, P., Irvine, W.T.M., Vitelli, V.: Odd elasticity. Nat. Phys. **16**, 475–480 (2020). https://doi.org/10.1038/s41567-020-0795-y
6. Chen, Y., Li, X., Scheibner, C., Vitelli, V., Huang, G.: Realization of active metamaterials with odd micropolar elasticity. Nat. Commun. **12**, 1–12 (2021). https://doi.org/10.1038/s41467-021-26034-z
7. Zhu, R., Liu, X.N., Hu, G.K., Sun, C.T., Huang, G.L.: A chiral elastic metamaterial beam for broadband vibration suppression. J. Sound Vib. **333**, 2759–2773 (2014). https://doi.org/10.1016/j.jsv.2014.01.009
8. Matlack, K.H., Bauhofer, A., Krödel, S., Palermo, A., Daraio, C.: Composite 3D-printed metastructures for lowfrequency and broadband vibration absorption. Proc. Natl. Acad. Sci. USA **113**, 8386–8390 (2016). https://doi.org/10.1073/pnas.1600171113
9. Cai, C., Zhou, J., Wu, L., Wang, K., Xu, D., Ouyang, H.: Design and numerical validation of quasi-zero-stiffness metamaterials for very low-frequency band gaps. Compos. Struct. **236**, 111862 (2020). https://doi.org/10.1016/j.compstruct.2020.111862
10. Zhang, M., Yang, J., Zhu, R.: Origami-based bistable metastructures for low-frequency vibration control. J. Appl. Mech., Transact. ASME **88**, 051009 (2021). https://doi.org/10.1115/1.4049953
11. Park, C.S., Shin, Y.C., Jo, S.H., Yoon, H., Choi, W., Youn, B.D., Kim, M.: Two-dimensional octagonal phononic crystals for highly dense piezoelectric energy harvesting. Nano Energy **57**, 327–337 (2019). https://doi.org/10.1016/j.nanoen.2018.12.026
12. Lu, Z.Q., Zhao, L., Ding, H., Chen, L.Q.: A dual-functional metamaterial for integrated vibration isolation and energy

harvesting. J. Sound Vib. **509**, 11625 (2021). https://doi.org/10.1016/j.jsv.2021.116251
13. Lee, G., Lee, D., Park, J., Jang, Y., Kim, M., Rho, J.: Piezoelectric energy harvesting using mechanical metamaterials and phononic crystals. Commun. Phys. **5**, 1–16 (2022). https://doi.org/10.1038/s42005-022-00869-4
14. Tan, K.T., Huang, H.H., Sun, C.T.: Blast-wave impact mitigation using negative effective mass density concept of elastic metamaterials. Int. J. Impact Eng **64**, 20–29 (2014). https://doi.org/10.1016/j.ijimpeng.2013.09.003
15. Hu, J., Yu, T.X., Yin, S., Xu, J.: Low-speed impact mitigation of recoverable DNA-inspired double helical metamaterials. Int. J. Mech. Sci. **161**, 105050 (2019). https://doi.org/10.1016/j.ijmecsci.2019.105050
16. Oudich, M., Assouar, M.B., Hou, Z.: Propagation of acoustic waves and waveguiding in a two-dimensional locally resonant phononic crystal plate. Appl. Phys. Lett. **97**, 65–68 (2010). https://doi.org/10.1063/1.3513218
17. Li, G.H., Wang, Y.Z., Wang, Y.S.: Active control on switchable waveguide of elastic wave metamaterials with the 3D printing technology. Sci. Rep. **9**, 1–8 (2019). https://doi.org/10.1038/s41598-019-52705-5
18. Tan, K.T., Huang, H.H., Sun, C.T.: Optimizing the band gap of effective mass negativity in acoustic metamaterials. Appl. Phys. Lett. **101**, 241902 (2012). https://doi.org/10.1063/1.4770370
19. Hu, G., Tang, L., Das, R., Gao, S., Liu, H.: Acoustic metamaterials with coupled local resonators for broadband vibration suppression. AIP Adv. **7**, 025211 (2017). https://doi.org/10.1063/1.4977559
20. Abdeljaber, O., Avci, O., Inman, D.J.: Optimization of chiral lattice based metastructures for broadband vibration suppression using genetic algorithms. J. Sound Vib. **369**, 50–62 (2016). https://doi.org/10.1016/j.jsv.2015.11.048
21. Yeh, S.L., Harne, R.L.: Origins of broadband vibration attenuation empowered by optimized viscoelastic metamaterial inclusions. J. Sound Vib. **458**, 218–237 (2019). https://doi.org/10.1016/j.jsv.2019.06.018
22. Wang, Z., Zhang, Q., Zhang, K., Hu, G.: Tunable digital metamaterial for broadband vibration isolation at low frequency. Adv. Mater. **28**, 9857–9861 (2016). https://doi.org/10.1002/adma.201604009
23. Yang, X.W., Lee, J.S., Kim, Y.Y.: Effective mass density based topology optimization of locally resonant acoustic metamaterials for bandgap maximization. J. Sound Vib. **383**, 89–107 (2016). https://doi.org/10.1016/j.jsv.2016.07.022
24. Yi, K., Matten, G., Ouisse, M., Sadoulet-Reboul, E., Collet, M., Chevallier, G.: Programmable metamaterials with digital synthetic impedance circuits for vibration control. Smart Mater. Struct. **29**, 035005 (2020). https://doi.org/10.1088/1361-665X/ab6693
25. Yi, K., Collet, M.: Broadening low-frequency bandgaps in locally resonant piezoelectric metamaterials by negative capacitance. J. Sound Vib. **493**, 115837 (2021). https://doi.org/10.1016/j.jsv.2020.115837
26. Wu, K., Hu, H., Wang, L.: Optimization of a type of elastic metamaterial for broadband wave suppression. Proc. Royal Soc. A Math. Phys. Eng. Sci. **477**, 20210337 (2021). https://doi.org/10.1098/rspa.2021.0337
27. Wu, K., Hu, H., Wang, L., Gao, Y.: Parametric optimization of an aperiodic metastructure based on genetic algorithm. Int. J. Mech. Sci. **214**, 106878 (2022). https://doi.org/10.1016/j.ijmecsci.2021.106878
28. Xu, X., Barnhart, M.V., Li, X., Chen, Y., Huang, G.: Tailoring vibration suppression bands with hierarchical metamaterials containing local resonators. J. Sound Vib. **442**, 237–248 (2019). https://doi.org/10.1016/j.jsv.2018.10.065
29. Zhao, P., Zhang, K., Zhao, C., Deng, Z.: Multi-resonator coupled metamaterials for broadband vibration suppression. Appl. Math. Mech. **42**, 53–64 (2021). https://doi.org/10.1007/s10483-021-2684-8
30. Wei, W., Ren, S., Chronopoulos, D., Meng, H.: Optimization of connection architectures and mass distributions for metamaterials with multiple resonators. J. Appl. Phys. **129**, 165101 (2021). https://doi.org/10.1063/5.0047391
31. Hu, G., Austin, A.C.M., Sorokin, V., Tang, L.: Metamaterial beam with graded local resonators for broadband vibration suppression. Mech. Syst. Signal Process. **146**, 106982 (2021). https://doi.org/10.1016/j.ymssp.2020.106982
32. Celli, P., Yousefzadeh, B., Daraio, C., Gonella, S.: Bandgap widening by disorder in rainbow metamaterials. Appl. Phys. Lett. **114**, 091903 (2019). https://doi.org/10.1063/1.5081916
33. Li, C., Jiang, T., He, Q., Peng, Z.: Stiffness-mass-coding metamaterial with broadband tunability for low-frequency vibration isolation. J. Sound Vib. **489**, 115685 (2020). https://doi.org/10.1016/j.jsv.2020.115685
34. Yi, K., Liu, Z., Zhu, R.: Multi-resonant metamaterials based on self-sensing piezoelectric patches and digital circuits for broadband isolation of elastic wave transmission. Smart Mater. Struct. **31**, 015042 (2022). https://doi.org/10.1088/1361-665X/ac3b1f
35. Ma, G., Sheng, P.: Acoustic metamaterials: from local resonances to broad horizons. Sci. Adv. **2**, e1501595 (2016). https://doi.org/10.1126/sciadv.1501595
36. Kovacic I., Brennan M. J.: The Duffing equation: nonlinear oscillators and their behaviour, John Wiley & Sons, (2011). https://doi.org/10.1002/9780470977859.
37. Holmes, P.J., Moon, F.C.: Strange attractors and chaos in nonlinear mechanics. J Appl. Mech. Transact. ASME **50**, 1021–1032 (1983). https://doi.org/10.1115/1.3167185
38. Szemplińska-Stupnicka, W.: Secondary resonances and approximate models of routes to chaotic motion in nonlinear oscillators. J. Sound Vib. **113**, 155–172 (1987). https://doi.org/10.1016/S0022-460X(87)81348-2
39. Nayfeh, A.H., Sanchez, N.E.: Bifurcations in a forced softening Duffing oscillator. Int. J. Non-Linear Mech. **24**, 483–497 (1989). https://doi.org/10.1016/0020-7462(89)90014-0
40. Balachandran, B., Nayfeh, A.H.: Nonlinear motions of beam-mass structure. Nonlinear Dyn. **1**, 39–61 (1990). https://doi.org/10.1007/BF01857584
41. Jing, X.J., Vakakis, A.F.: Exploring nonlinear benefits in engineering. Mech. Syst. Signal Process. **125**, 1–3 (2019). https://doi.org/10.1016/j.ymssp.2019.01.059
42. Kovacic I., Lenci S.: IUTAM symposium on exploiting nonlinear dynamics for engineering systems, Springer, (2019). https://doi.org/10.1007/978-3-030-23692-2.

43. Cabaret, J., Tournat, V., Béquin, P.: Amplitude-dependent phononic processes in a diatomic granular chain in the weakly nonlinear regime. Phys. Rev. E–Stat. Nonlinear Soft Matter Phys. **86**, 1–10 (2012). https://doi.org/10.1103/PhysRevE.86.041305
44. Manktelow, K.L., Leamy, M.J., Ruzzene, M.: Analysis and experimental estimation of nonlinear dispersion in a periodic string. J. Vib. Acoust., Transact ASME **136**, 1–8 (2014). https://doi.org/10.1115/1.4027137
45. Chakraborty, G., Mallik, A.K.: Dynamics of a weakly nonlinear periodic chain. Int. J. Non-Linear Mech. **36**, 375–389 (2001). https://doi.org/10.1016/S0020-7462(00)00024-X
46. Narisetti, R.K., Leamy, M.J., Ruzzene, M.: A perturbation approach for predicting wave propagation in one-dimensional nonlinear periodic structures. J. Vib. Acoust. Transact. ASME **132**, 0310011–03100111 (2010). https://doi.org/10.1115/1.4000775
47. Konarski, S.G., Haberman, M.R., Hamilton, M.F.: Frequency-dependent behavior of media containing prestrained nonlinear inclusions: application to nonlinear acoustic metamaterials. J. Acoust. Soc. Am. **144**, 3022–3035 (2018). https://doi.org/10.1121/1.5078529
48. Meaud, J.: Nonlinear wave propagation and dynamic reconfiguration in two-dimensional lattices with bistable elements. J. Sound Vib. **473**, 115239 (2020). https://doi.org/10.1016/j.jsv.2020.115239
49. Fang, X., Wen, J., Bonello, B., Yin, J., Yu, D.: Wave propagation in one-dimensional nonlinear acoustic metamaterials. New J. Phys. **19**, 053007 (2017). https://doi.org/10.1088/1367-2630/aa6d49
50. Luo, B., Gao, S., Liu, J., Mao, Y., Li, Y., Liu, X.: Nonreciprocal wave propagation in one-dimensional nonlinear periodic structures. AIP Adv. **8**, 015113 (2018). https://doi.org/10.1063/1.5010990
51. Li, Z.-N., Wang, Y.-Z., Wang, Y.-S.: Tunable mechanical diode of nonlinear elastic metamaterials induced by imperfect interface. Pro Royal Soc. A. **477**, 20200357 (2021). https://doi.org/10.1098/rspa.2020.0357
52. Fraternali, F., Senatore, L., Daraio, C.: Solitary waves on tensegrity lattices. J. Mech. Phys. Solids **60**, 1137–1144 (2012). https://doi.org/10.1016/j.jmps.2012.02.007
53. Fraternali, F., Carpentieri, G., Amendola, A., Skelton, R.E., Nesterenko, V.F.: Multiscale tunability of solitary wave dynamics in tensegrity metamaterials. Appl. Phys. Lett. **105**, 201903 (2014). https://doi.org/10.1063/1.4902071
54. Manktelow, K., Leamy, M.J., Ruzzene, M.: Multiple scales analysis of wave-wave interactions in a cubically nonlinear monoatomic chain. Nonlinear Dyn. **63**, 193–203 (2011). https://doi.org/10.1007/s11071-010-9796-1
55. Lazarov, B.S., Jensen, J.S.: Low-frequency band gaps in chains with attached non-linear oscillators. Int. J. Non-Linear Mech. **42**, 1186–1193 (2007). https://doi.org/10.1016/j.ijnonlinmec.2007.09.007
56. Lepidi, M., Bacigalupo, A.: Wave propagation properties of one-dimensional acoustic metamaterials with nonlinear diatomic microstructure. Nonlinear Dyn. **98**, 2711–2735 (2019). https://doi.org/10.1007/s11071-019-05032-3
57. Fortunati, A., Bacigalupo, A., Lepidi, M., Arena, A., Lacarbonara, W.: Nonlinear wave propagation in locally dissipative metamaterials via Hamiltonian perturbation approach. Nonlinear Dyn. **108**, 765–787 (2022). https://doi.org/10.1007/s11071-022-07199-8
58. Xu, X., Barnhart, M.V., Fang, X., Wen, J., Chen, Y., Huang, G.: A nonlinear dissipative elastic metamaterial for broadband wave mitigation. Int. J. Mech. Sci. **164**, 105159 (2019). https://doi.org/10.1016/j.ijmecsci.2019.105159
59. Bae, M.H., Oh, J.H.: Nonlinear elastic metamaterial for tunable bandgap at quasi-static frequency. Mech. Syst. Signal Process. **170**, 108832 (2022). https://doi.org/10.1016/j.ymssp.2022.108832
60. Xia, Y., Ruzzene, M., Erturk, A.: Dramatic bandwidth enhancement in nonlinear metastructures via bistable attachments. Appl. Phys. Lett. **114**, 093501 (2019). https://doi.org/10.1063/1.5066329
61. Xia, Y., Ruzzene, M., Erturk, A.: Bistable attachments for wideband nonlinear vibration attenuation in a metamaterial beam. Nonlinear Dyn. **102**, 1285–1296 (2020). https://doi.org/10.1007/s11071-020-06008-4
62. Silva, P.B., Leamy, M.J., Geers, M.G.D., Kouznetsova, V.G.: Emergent subharmonic band gaps in nonlinear locally resonant metamaterials induced by autoparametric resonance. Phys. Rev. E **99**, 1–14 (2019). https://doi.org/10.1103/PhysRevE.99.063003
63. Zega, V., Silva, P.B., Geers, M.G.D., Kouznetsova, V.G.: Experimental proof of emergent subharmonic attenuation zones in a nonlinear locally resonant metamaterial. Sci. Rep. **10**, 1–11 (2020). https://doi.org/10.1038/s41598-020-68894-3
64. Fang, X., Wen, J., Bonello, B., Yin, J., Yu, D.: Ultra-low and ultra-broad-band nonlinear acoustic metamaterials. Nat. Commun. **8**, 1–11 (2017). https://doi.org/10.1038/s41467-017-00671-9
65. Wu, K., Hu, H., Wang, L.: Nonlinear elastic waves in a chain type of metastructure: theoretical analysis and parametric optimization. Nonlinear Dyn. (2023). https://doi.org/10.1007/s11071-023-08413-x
66. Shen, Y., Lacarbonara, W.: Nonlinear dispersion properties of metamaterial beams hosting nonlinear resonators and stop band optimization. Mech. Syst. Signal Process. **187**, 109920 (2023). https://doi.org/10.1016/j.ymssp.2022.109920
67. Shen, Y., Lacarbonara, W.: Nonlinearity enhanced wave bandgaps in metamaterial honeycombs embedding spider web-like resonators. J Sound Vib. **562**, 117821 (2023). https://doi.org/10.1016/j.jsv.2023.117821
68. Fang, X., Wen, J., Benisty, H., Yu, D.: Ultrabroad acoustical limiting in nonlinear metamaterials due to adaptive-broadening band-gap effect. Phys. Rev. B **101**, 1–10 (2020). https://doi.org/10.1103/PhysRevB.101.104304
69. Gong, C., Fang, X., Cheng, L.: Band degeneration and evolution in nonlinear triatomic metamaterials. Nonlinear Dyn. **2**, 1–16 (2022). https://doi.org/10.1007/s11071-022-07860-2
70. Chen, Y.Y., Barnhart, M.V., Chen, J.K., Hu, G.K., Sun, C.T., Huang, G.L.: Dissipative elastic metamaterials for broadband wave mitigation at subwavelength scale. Compos. Struct. **136**, 358–371 (2016). https://doi.org/10.1016/j.compstruct.2015.09.048
71. Bukhari, M., Barry, O.: Spectro-spatial analyses of a nonlinear metamaterial with multiple nonlinear local

resonators. Nonlinear Dyn. **99**, 1539–1560 (2020). https://doi.org/10.1007/s11071-019-05373-z
72. Krack M., Gross J.: Harmonic balance for nonlinear vibration problems, Springer, 2019. https://doi.org/10.1007/978-3-030-14023-6.
73. Malatkar, P., Nayfeh, A.H.: Steady-State dynamics of a linear structure weakly coupled to an essentially nonlinear oscillator. Nonlinear Dyn. **47**, 167–179 (2007). https://doi.org/10.1007/s11071-006-9066-4
74. Zhang, Y., Kong, X., Yue, C., Xiong, H.: Dynamic analysis of 1-dof and 2-dof nonlinear energy sink with geometrically nonlinear damping and combined stiffness. Nonlinear Dyn. **105**, 167–190 (2021). https://doi.org/10.1007/s11071-021-06615-9